ACS NANO
Cite This: ACS Nano XXXX, XXX, XXX−XXX
www.acsnano.org

ARTICLE

Atomic Structure and Dynamics of Self-Limiting Sub-Nanometer Pores in Monolayer WS_2

Gyeong Hee Ryu,[†] Arthur France-Lanord,[‡] Yi Wen,[†] Si Zhou,[†] Jeffrey C. Grossman,[‡] and Jamie H. Warner*[,†]

[†]Department of Materials, University of Oxford, 16 Parks Road, Oxford OX1 3PH, United Kingdom

[‡]Department of Materials Science and Engineering, Massachusetts Institute of Technology, 77 Massachusetts Avenue, Cambridge, Massachusetts 02139, United States

Supporting Information

ABSTRACT: We reveal a self-limiting mechanism during the formation of a specific type of circular nanopore in monolayer WS_2 that limits its diameter to sub-nm. A single W atom vacancy (triangular nanopore) is transformed into the self-limiting nanopore (SLNP) through the atomic restructuring of S atoms around the area, reducing the number of dangling bonds at the nanopore edge by shifting them further in-plane with W−W bonding instead. Bond rotations in WS_2 help accommodate the electron beam induced atomic loss and ensure the stability of the SLNP. The SLNP shows significant improvement in diameter stability during electron beam irradiation compared to other triangular nanopores in WS_2 that typically continue to expand in diameter during atom loss. The atomic structure of these SLNPs is studied using aberration-corrected scanning transmission electron microscopy with an *in situ* heating holder, revealing that the SLNPs are mostly formed at a temperature of ∼500 °C, which is a balance between thermally activated S vacancy diffusion and sufficient S vacancy density to initiate local atomic reconstruction. At higher temperatures (*i.e.*, 1000 °C), S vacancies quickly migrate away into long line vacancies, resulting in low S vacancy density and rapidly expanding holes generated at the edges of the line vacancies. At room temperature, S vacancy migration is low and vacancy density is very high, which limits atomic reconstruction, and instead many small holes open up. These results provide insights into the factors that lead to uniform sized nanopores in the sub-nm range in transition-metal dichalcogenides.

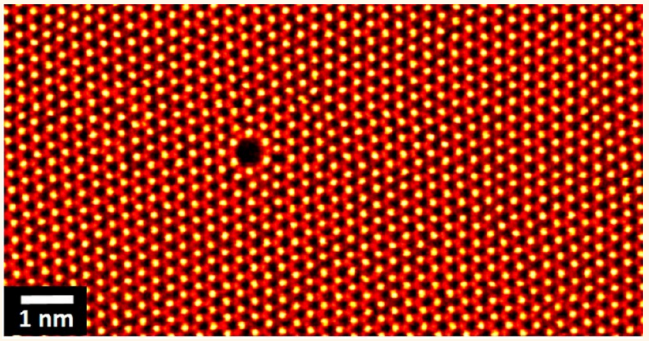

KEYWORDS: *nanopore, bond rotation, WS_2, 2D materials, scanning transmission electron microscopy*

Nanopores in membranes have become increasingly important for applications in gas filtration,[1−6] water purification,[7−11] solution-based separation methods, and biomolecular recognition during nanopore translocation.[12−18] Two-dimensional (2D) materials offer ideal membrane platforms due to their monolayer thickness and have been explored in the forms of graphene[12,19−22] and transition-metal dichalcogenides (TMDs) of MoS_2.[23] Research into nanopores in 2D materials for DNA translocation measurement has revealed that TMDs are more stable compared to graphene.[17,18] Nanopores are the intermediate between large holes and small point vacancies, with their formation enabled by the removal of atoms from the lattice by methods such as electron beam irradiation,[24−26] electrochemical etching,[27] and ion irradiation.[28]

The detailed atomic structure of nanopores in 2D materials has been studied by transmission electron microscopy,[24,29,30] often *in situ* after their creation by controlled electron beam irradiation. Sub-nanometer pores in graphene were studied by low-voltage aberration-corrected TEM using an *in situ* high-temperature holder, which prevented mobile surface carbon from filling the nanopores.[24] The high strain from the circular geometry of the sub-nm pore prevented reconstruction and bond rotations from occurring at the edges when compared to long linear edge regions in graphene. In MoS_2, nanometer pores have been created on-demand with 5 nm spacings by controlling the angstrom-sized focus electron beam during

Received: September 14, 2018
Accepted: October 22, 2018

DOI: 10.1021/acsnano.8b07051
ACS Nano XXXX, XXX, XXX−XXX

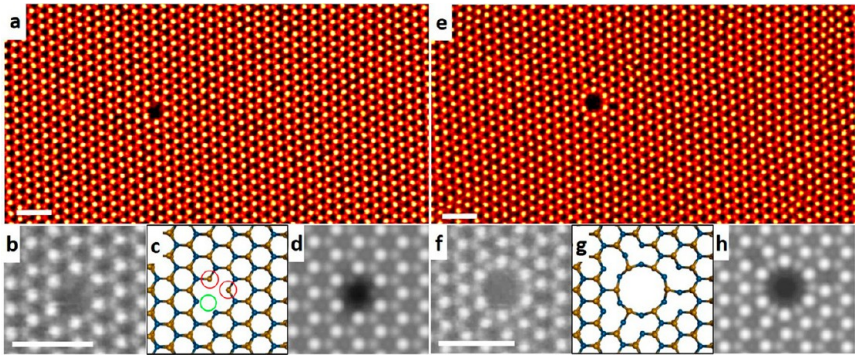

Figure 1. (a) and (e) ADF-STEM images of a triangular nanopore and a circular SLNP in monolayer WS_2 at 500 °C. (b) and (f) Higher magnification images of (a) and (e). (c) and (g) Corresponding atomic models. Orange atoms indicate S, and blue atoms indicate W in the atomic models. Red circles in (c) indicate 1S sites and green circle indicates 2S vacancy. (d) and (h) Multislice ADF-STEM image simulations corresponding to the circular and triangular nanopore atomic models in (c) and (g). Scale bars are 1 nm.

scanning transmission electron microscopy at the low accelerating voltage of 60 kV.[31] The formation of nanopores in MoS_2 down to single Mo atom vacancies was enabled by the sputtering of S atoms by the electron beam, which destabilizes the Mo bonding and causes Mo atoms to migrate to the surface and diffuse away from the nanopore.[32] However, sub-nm pores within MoS_2 that are formed by the loss of a single Mo atom are prone to healing by filling from mobile Mo atoms, either by self-healing from the same atom that has not migrated sufficiently far enough away or from other migrating Mo species from elsewhere in the sample. This makes sub-nm pores in TMDs relatively unstable, and this poses an issue for their continual use in applications. Developing ways to create stable nanopores in 2D materials is therefore crucial for their continual development.

In graphene, this has been achieved by the decoration of the edges by foreign atoms such as Si,[29] or by forming bilayer closed edge structures that seal up the dangling bonds at the edges of monolayer graphene nanopores.[26] This stops surface carbon contamination from filling the graphene nanopores. However, for nanopores in TMDs, filling with carbon contamination is not as frequent as in graphene, but the issue of dangling bonds still remains, along with the challenge of stabilizing sub-nm pores from metal filling and healing.

Here, we reveal a stable self-limiting nanopore (SLNP) in the TMD monolayer WS_2, which is circular and forms around a single missing W atomic site. Annular dark-field scanning transmission electron microscopy (ADF-STEM) is used to study the detailed atomic structure of the circular SLNP and shows it has a higher stability to electron beam induced enlargement and resistance against filling by mobile W atoms compared to nonreconstructed nanopores. Structural relaxations are examined by using density functional theory (DFT) and multislice image simulations to confirm the match to experimental observations. An *in situ* heating holder is used to show how thermal energy activation of S vacancy diffusion and atomic reconstruction plays a major role in the nanopore formation. We also use the temperature-dependent observations of trigonal bond rotated defects, often called trefoil defects, that were previously observed in WSe_2 and mentioned to be present in WS_2,[33] to understand the role of W–W bonding stability at the critical temperature of 500 °C, similar to SLNP formation.

RESULTS AND DISCUSSION

WS_2 is grown by chemical vapor deposition and transferred to an *in situ* heating chip for TEM that contains Si_3N_4 thin film with slits cut in by focused ion beam. The *in situ* heating holder enables temperatures up to 1000 °C to be studied with atomic resolution. ADF-STEM imaging is performed at an accelerating voltage of 60 kV to minimize damage. Generally, at high temperatures >500 °C, the surface of monolayer WS_2 is cleaner than at room temperature because of the evaporation of the amorphous surface carbon. At room temperature, S vacancy mobility is low and S vacancies form in high density from electron beam induced atomic loss. This results in lots of small nanopores forming in a small area, and these then enlarge rapidly, once they form. In some cases, if the nanopore formed is only from the loss of one W atom, it can self-heal, provided the displaced W atom has not migrated away from the rim of the nanopore.

At high temperatures, 700–1000 °C, the S vacancies in TMDs are thermally activated and rapidly migrate to form long line defects (Figure S1c,d).[34−37] The rapid migration of the S vacancies away from the irradiation area to join an existing long line vacancy means the majority of the WS_2 has low vacancy density. Nanopores then typically form at the edges of line defects or surface bound atoms and enlarge rapidly once created (Figure S1e,f). The need for bond rotations or atomic reconstruction is reduced because the majority of S vacancies just increase the length of an existing long line vacancy. This makes it difficult to observe stable sub-nm pores at such high temperatures, because once a nanopore opens, it rapidly loses atoms from its edge region. However, heating the WS_2 at 500 °C provides a balance of sufficient thermal energy for small-scale S vacancy migration and atomic reconstruction and the buildup of local S vacancy density. The three-bond rotational defects are also commonly observed at this temperature (Figure S1a,b).[33] Our findings reveal that the thermal energy in the system needs to be sufficient to allow some S vacancy migration and bond rotation, but not so large that S vacancies diffuse so rapidly away from the local area.

Figure 1 shows the ADF-STEM images capturing the transformation of a triangular nanopore into the circular SLNP, at 500 °C by atomic reconstructions and additional S atom loss. DFT relaxed atomic models are used for multislice ADF-STEM image simulations and are compared to the experimental images (Figure 1c,d and g,h), showing excellent match. The triangular nanopore in Figure 1a–c consists of

DOI: 10.1021/acsnano.8b07051
ACS Nano XXXX, XXX, XXX–XXX

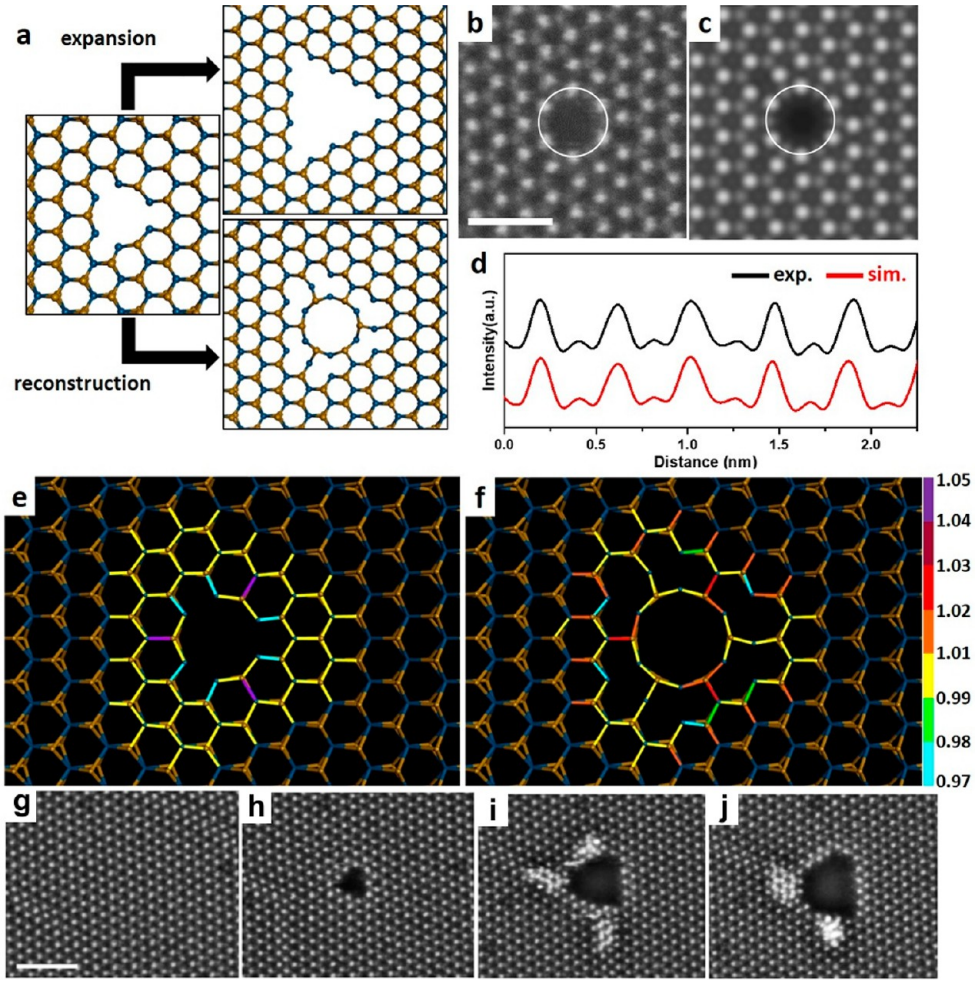

Figure 2. (a) Schematic illustration showing the formation of an extended triangular hole and a circular SLNP from a triangular nanopore missing one W and six S atoms. Orange atoms indicate S, and blue atoms indicate W. (b) ADF-STEM image showing a circular nanopore. (c) Multislice ADF-STEM image simulation corresponding to the circular atomic model in (a). (d) Intensity profiles measured from atomic arrangements at the edge of the circular nanopore in (b) and (c). The trace corresponds to the white circled paths in (b) and (c). (e) and (f) Atomic models of the triangular nanopore and circular SLNP showing the ratio of local bond length to the average bond length of pristine WS_2 based on DFT. Scale bar is 1 nm. The warm colors (orange, red, purple, and violet) indicate bond elongation, and the cold colors (yellow-green and sky-blue) indicate the contraction of a bond. (g–j) Successive ADF-STEM images of the formation and expansion of a triangular nanopore at 500 °C in monolayer WS_2. This image shows that the nanopore newly formed is expanded. Scale bar is 2 nm. Time between frames is ~30 s.

missing single W atom and several of its surrounding S atoms, leaving many dangling bonds at the edge. The transformation into the circular SLNP, then reduces the amount of dangling bonds at the edge. The diameter of the circular SLNP was measured as 0.72 nm (Figure S2).

Removing a single W atom and some nearest-neighbor S atoms from monolayer WS_2 by electron beam irradiation generally occurs by first S atomic loss and then W atom displacement to the surface of WS_2 and followed by W migration away from the nanopore.[31] Further electron beam irradiation then can expand the size of the hole by further atomic loss of atoms from the edge, which has a lower energy threshold. Figure 2a shows two ways a sub-nm pore evolves under electron irradiation, either the nanopore expands, as shown in Figure 2g–j or it reconstructs into the SLNP, as in Figure 1a,b. Because the formation of the SLNP from the initial triangular nanopore is complex and requires further S atomic loss, there are statistical variations that mean it does not occur 100% of the time. This is true for all stochastic processes driven by electron beam atomic loss. So we included the example presented in Figure 2g–j to show the case when the nanopore simply just expands. This will be due to the electron beam sputtering atoms from the edge of the nanopore in a random matter, instead of sputtering atoms from the local lattice surrounding the nanopore. The observation in Figure 2g–j is typical for nearly all temperatures and also for MoS_2. The temperature conditions of 500 °C are ideal in WS_2 to lead to the SLNP formation, and we explain why this is the case later in the discussion, which is because of the balance between thermally activated S vacancy diffusion and local S vacancy density at different temperatures. The extra atoms in Figure 2i,j are W atoms, and this is because the hole is large. S atoms are easily removed by the electron beam, but W atoms stay attached to the local area and give this contrast. For small sub-nm pores, typically they are only stable if the W atom has migrated away from the hole and is therefore not able to backfill it by self-healing. This is why the sub-nm pores (Figure 2h) do not have extra atoms around their edge.

DOI: 10.1021/acsnano.8b07051
ACS Nano XXXX, XXX, XXX–XXX

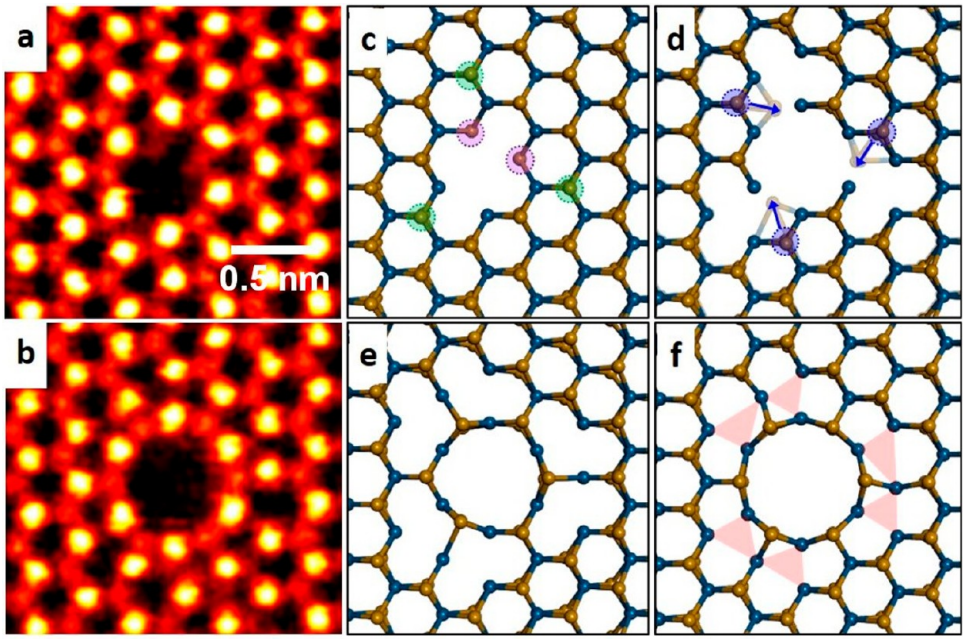

Figure 3. Formation of a circular SLNP from a triangular nanopore. (a) and (b) ADF-STEM images of a triangular and a circular nanopore, with (c) and (e) showing the corresponding matching relaxed DFT models, respectively. (c–f) The circular nanopore formation mechanisms, with highlighted atomic displacements driving the process. Green circles indicate S pairs, and violet circles indicate one S atom. Blue circles indicate migrating S pairs. Red shadings indicate W metal bonding sites. Orange and blue atoms, respectively, indicate S and W atoms in the atomic models. Scale bar is 0.5 nm.

Importantly, S atoms located at the edge of the SLNP have no dangling bonds as in the case of the triangular nanopore (Figure 2b). Figure 2c shows a multislice ADF-STEM image simulation that matches Figure 2b. Intensity line profiles at the edge of the circular SLNP, indicated by white circled lines in Figure 2b,c, are measured for both experimental and simulated ADF-STEM images, showing good agreement (Figure 2d). The ADF-STEM image indicates that this SLNP nanopore is made of a repeating unit consisting of an S pair and a W atom. The colored bonds shown in the atomic models (Figure 2e,f) visually illustrate the bond length variations around the triangular and circular pores, with the values calculated by dividing every measured or calculated bond length around the nanopore by a reference bond distance. For the triangular pore (Figure 2e), elongation is only detected in the bonds which are perpendicular to the middle of the edge (violet lines), and compression is detected at the bonds next to the corners of the nanopore (indicated by sky-blue lines). The other bonds are relatively uniform in length. On the other hand, elongation in the circular SLNP is mainly detected at positions where the S pairs constituting the SLNP are bonded to the W atoms of the existing lattice. Compression is only detected at the boundary bonds between the existing lattice and uneven decagons (Figure 2f). The formation mechanisms are presented in Figure 3.

To form a circular SLNP from a triangle nanopore (Figures 3a,b), two S atoms inside the pore (violet circles) and three S pairs located at the corner of the nanopore are removed, which are indicated by green dashed circles as shown in Figure 3c. Following that, three S pairs indicated by blue circles shift inside the nanopore along the blue arrows (Figure 3d). The structure then finally relaxes into the SLNP (Figure 3b,f). In order to create a circular nanopore from a triangular nanopore as in Figure 3a,b, three S pairs, which are indicated by green circles or blue circles, must be removed from the pore or S vacancies must be migrated to designated positions of the corner. Next, the other three pairs also shift as shown in Figure 3d at the side of the triangular nanopore. At the edge side structure of the triangular nanopore (Figure 2a), the S pairs are bonded to three W atoms with no dangling bonds, and the W atoms at the edge are bonded to two S pairs each. This is also the case for the circular SLNP; however, in this case of the SLNP, the edge is composed of uneven rings and of the atoms consisting of the uneven pairs of the edge. In these rings, three W atoms form metal sites (red shadings in Figure 3f). And as shown in Figures 3e,f, upon relaxation, a circular nanopore is formed, and distances among the metal atoms become closer. Thus, these sites appear to interact with each other and play an important role in the SLNP remaining stable under electron beam irradiation, unlike the triangular nanopore.

DFT calculations confirm the experimental observation that the triangular nanopore is able to transform into a circular SLNP as shown in Figure 3. Table S1 lists the formation energies of various nanopores in the Supporting Information. A new nanopore structure (Tri-6S), which has the same stoichiometry as the circular nanopore, is considered to confirm that the formation of a circular nanopore is energetically more favorable than the Tri-6S. Starting from the triangular hole, the six closest S atoms are removed at the side of the hole leading to the formation of larger triangular structure (Figures S3a–c). In this case, it has larger formation energy than the circular nanopore, which shows that a circular nanopore is a more reasonable structure to form than expanded triangular nanopore. The pink shaded areas in Figure 3f highlight the W–W metal bonding region that is crucial in stabilizing this system in W-based TMDs.

The dynamics of nanopore formation in WS_2 was explored across a wide range of temperatures, and Figure 4 shows typical examples at room temperature (Figure 4a–i orange box), 700 °C (Figure 4j–m red box), and 1000 °C (Figure

DOI: 10.1021/acsnano.8b07051
ACS Nano XXXX, XXX, XXX–XXX

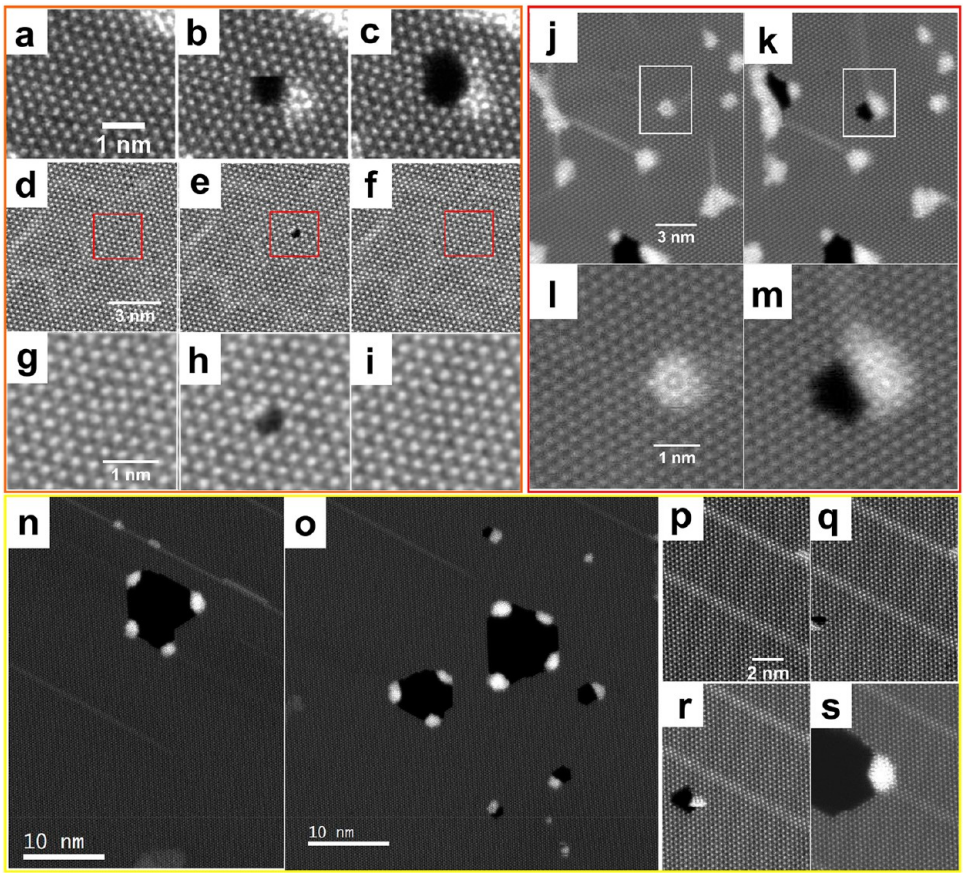

Figure 4. ***In situ*** **nanopore formation at different temperatures. Orange box (a–i) indicates room temperature, red box (j–m) 700 °C, and yellow box (n–s) 1000 °C. (a–c) Time series of ADF-STEM images showing nanopore formation at room temperature. 30 s between frames. (d) Time series of ADF-STEM images showing sub-nm pore formation and self-healing at room temperature. 30 s between frames. (g–i) Magnified view from red boxes in (d–f). (j) and (k) Sequential ADF-STEM images showing the nanopore formation at the line defect area containing surface W species (700 °C). (l) and (m) Magnified view of the white boxes in (j) and (k), revealing the zigzag faceted nanopore termination. (n) and (o) Two ADF-STEM images (2 min apart), showing nanopore formation at 1000 °C. (p) and (q) Time series of ADF-STEM images showing nanopore formation in WS_2 and rapid enlargement at 1000 °C. Time between frames is ∼30 s.**

4n–s yellow box). At room temperature, nanopores rapidly expand once created, without any well-defined faceted edging and appear circular (Figure 4a–c). In many cases, sub-nm pores are metastable and self-heal due to the inability of the ejected W atom to migrate away from the vacancy (Figure 4d–i) due to insufficient thermal energy for diffusion. At temperatures above 500 °C, such as 700 °C (Figure 4j–m) and 1000 °C (Figure 4n–s), the S vacancy diffusion is rapid, and the nanopores rapidly expand once formed. The edges are faceted along zigzag direction (Figure 4m). At this high temperature, the majority of the lattice is defect free, because the S vacancies have quickly migrated to the ultralong line defects. This lack of buildup of S point vacancies in the lattice is one of the crucial factors for the absence of the SLNP at these high temperatures, and the low migration energy at room temperature also prevents S vacancy rearrangement for SLNP formation, but at 500 °C, the balance between migration energy and S vacancy build-up is reached to provide ideal conditions to achieve SLNPs in WS_2.

During our temperature-dependent investigation, we found that the frequent observations of the SLNP also correlated with the appearance of trigonal bond rotational (TBR) defects, seen at 500 °C, but rarely at 700 and 1000 °C or at room temperature. Hexagonal 2D materials composed of heterogeneous atoms rarely undergo Stone–Wales transformation, although frequently formed in graphene, but TBR defects centered on a metal atom in WSe_2 have been reported.[12] The formation of TBR defects also requires W–W metal bonding regions, similar to SLNPs. TBR defects are classified into three types, depending on the presence or absence of chalcogen vacancies, and can be extended to line defects.[12] Figure 5 shows the formation of a TBR defect in a WS_2 at 500 °C under similar conditions to those that lead to SLNPs. S vacancies can easily form at random positions due to electron irradiation, as shown in Figure 5a, and these are able to migrate slightly more than at room temperature.[12] When six S vacancies assemble into a cluster of three S divacancies, the TBR defect occurs at the middle position by a 60° rotation of three bonds, indicated by the red circle in Figure 5d. Under continuous electron beam irradiation, the TBR defect does not migrate elsewhere but rather disappears completely *via* a 60° rotation of three bonds, indicated by the red circle in Figure 5e. The S divacancies can be seen again, as shown in Figure 5c,f. The vacancies are able to migrate somewhere else, and the bond rotation is also able to occur at the different position as shown in Figure 5g,j. In Figure 5h, the TBR defect is composed of two leaf-like structures (see also Figure 5k). Intuitively, the TBR defect seems to be formed straightforwardly through a 60° rotation, but it actually has an intermediate state as shown in Figure 5h,k, which is initiated when a S pair, indicated by a red dashed

DOI: 10.1021/acsnano.8b07051
ACS Nano XXXX, XXX, XXX–XXX

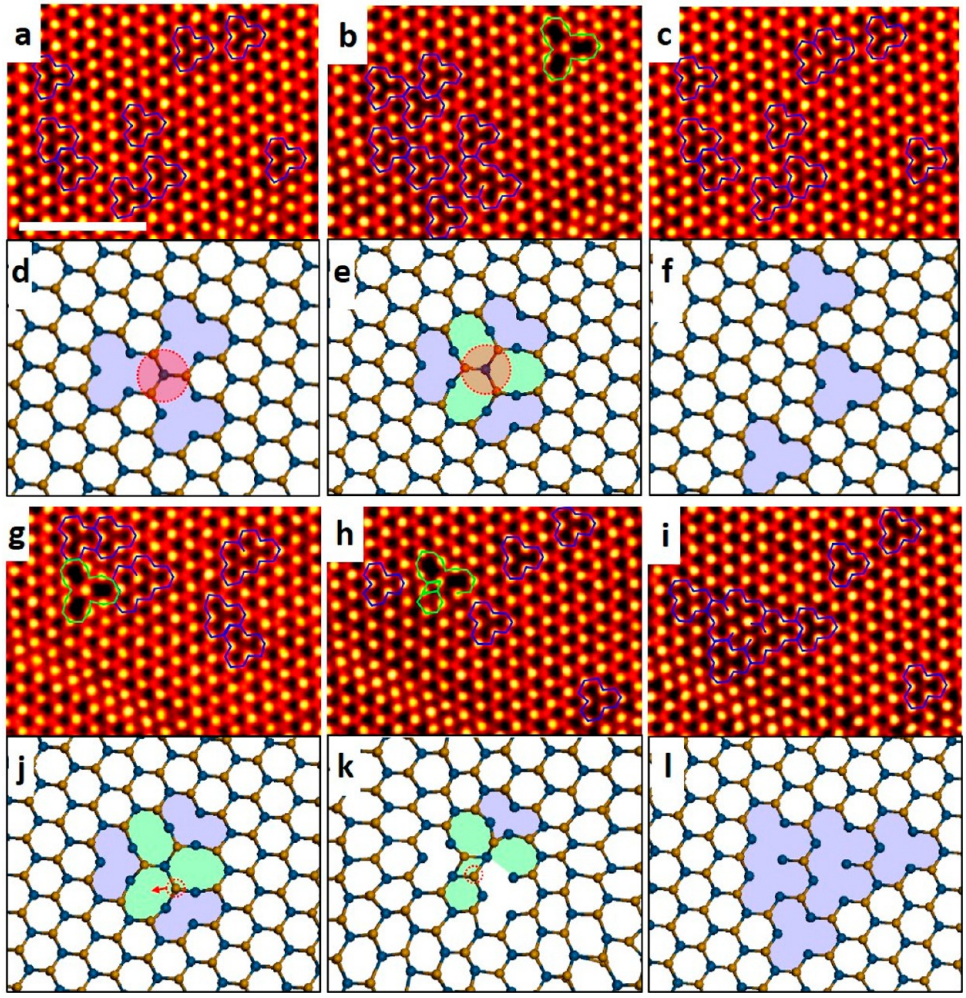

Figure 5. Time series of ADF-STEM images at 500 °C showing the formation of trigonal bond rotational defects repeatedly, with corresponding atomic models. The time between images is ~15 s. (a–l) STEM images and atomic models showing the appearance and disappearance of a trefoil defect by a 60° rotation of a trigonal bond. Green lines indicate the trefoil defects in (b) and (g) and the intermediate state in (h). Red circles in (d) and (e) indicate the positions where bond rotation occurs. Blue lines indicate S vacancies. (h) and (k) The intermediate state to the formation of the rotational defect, featuring two leaf-like structures. Red dashed circles indicate S pairs in (j) and (k). (i) and (l) Restored hexagonal lattices with S vacancies. In the atomic models, orange and blue atoms, respectively, indicate S and W atoms. Scale bar is 2 nm.

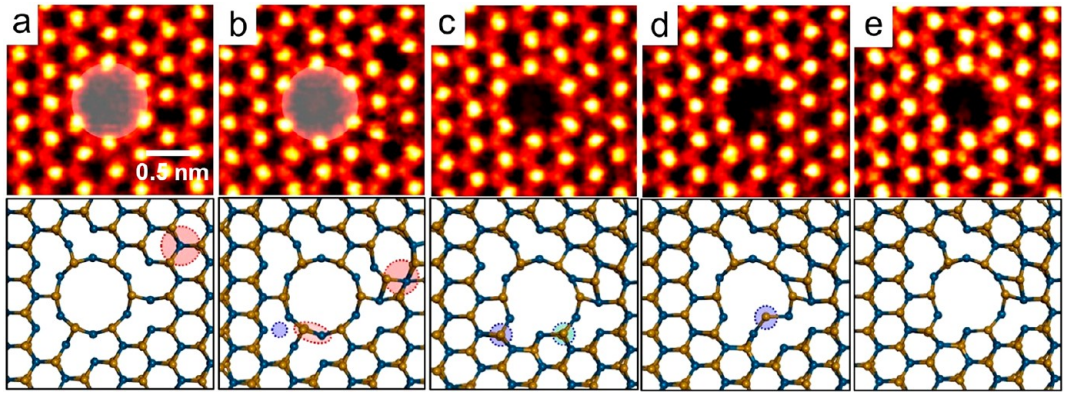

Figure 6. (a–e) Sequential ADF-STEM images showing the dynamics of a circular SLNP under continued electron beam irradiation, with associated atomic models show below each image. Time between images is ~30 s. Temperature is 500 °C. The atomic models show the dynamics occurring in this process. Red circles indicate the position of bond rotations, and the red oval indicates a Stone–Wales transformation in (a) and (b). Blue circles indicate the position of an S pair added to the system from (b) to (d), respectively.

circle in Figure 5j, is shifted along the red arrow. This S pair forms new bonds with three W atoms as shown in Figure 5k. If these transformations occur continuously, then isolated S vacancies can be observed without the TBR defects as shown

DOI: 10.1021/acsnano.8b07051
ACS Nano XXXX, XXX, XXX–XXX

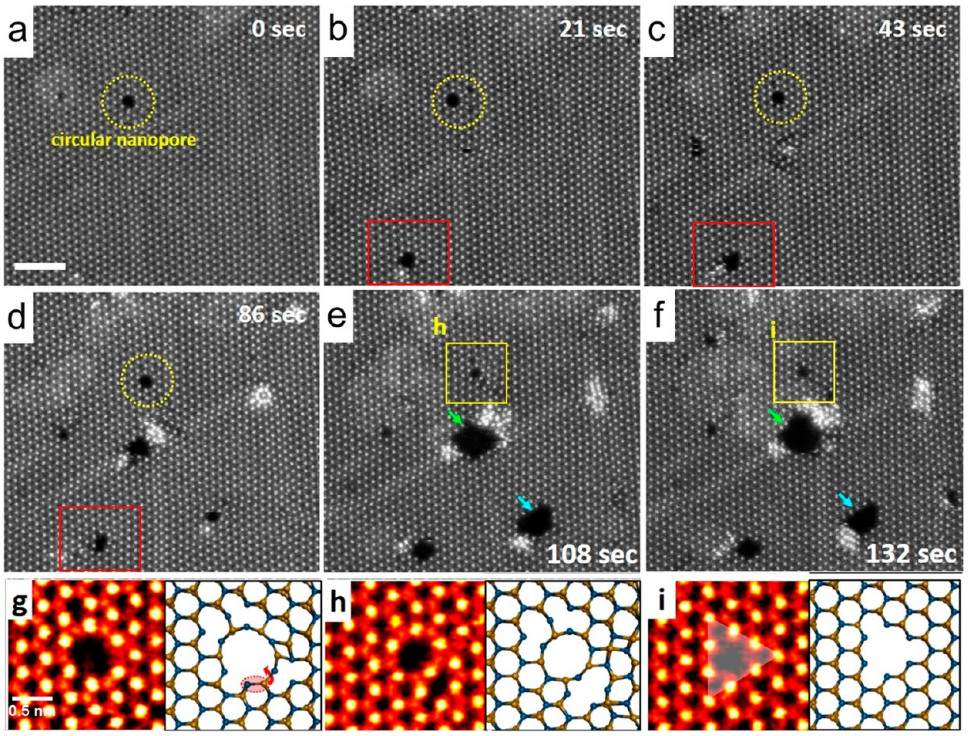

Figure 7. (a–f) Time series of ADF-STEM images showing the stability of a circular SLNP under continued electron beam irradiation and defect production at 500 °C. Yellow circles in (a–d) indicate the SLNP. Red boxes in (a–f) show another non-SLNP forming and enlarging. Green and cyan arrows in (e) and (f) show other large nanopores that formed. (g–i) ADF-STEM images of the nanopore, which are magnified images of the yellow circle and boxed regions, respectively, in (d–f), with atomic models showing the transition from the circular SLNP to a triangular pore. Scale bar in (a) is 2 nm.

in Figure 5i,l. Under our conditions we did not observe extended TBR defects, as reported in prior work on WSe_2,[33] but instead found them to disappear and reform and finally end up restoring to the hexagonal lattice. This may be due to the difference in W–S bonding compared to W–Se. During the dynamics shown in Figure 5, there was no noticeable shrinkage by the formation of extended long line defects or extended holes.[37] That means that the bond rotation can occur frequently instead of atom losses causing lattice shrinkages under given conditions. Furthermore, we also found a defect which has a very similar shape to that shown in Figure 4h,k, but it is not perfectly symmetric (see Figure S6). The formation of the trefoil defect (Figure 4b) results in the same W–W metal bonding rich areas as seen in the circular SLNPs. This suggests that W-based TMDs can accommodate different defect models in the lattice compared to Mo-based TMDs due to stronger W–W bonding compared to Mo–Mo bonding, explaining why SLNPs and trefoil defects are not observed in MoS_2 under similar conditions.[33]

Bond rotations are also found to occur around existing SLNPs, helping to maintain the stability of the SLNPs against further enlargement in size during continuous electron beam irradiation (Figure 6). The bonds indicated by a red dashed circle in the atomic model of Figure 6a are rotated as with the TBR defect. Additionally, another bond rotation and a Stone–Wales transformation occur counterclockwise at the positions indicated by the red circle and the red oval in the atomic model of Figure 6b. An S pair is added at the position indicated by the blue dashed circle. At this point, a Stone–Wales transformation could occur as it preserves both the three-fold symmetry and the polar nature of each bond. In Figure 6c, the blue circle indicates a missing S atom, and the green circle points to an S atom moving toward the pore, as shown in the atomic model of Figure 6d. Once the S atom which had moved at the previous step comes back to its original position and another S atom migrates to the same position, the structure shown in Figure 6e is formed. The newly created S vacancies around the SLNP are accommodated by local reconstructions, including bond rotations, rather than the SLNP getting larger. Figure 6c–e shows that some parts of the edge of the SLNP can have missing S atoms, but it quickly reconstructs by S atoms migrating from the inner region to the edge to seal up the vacancy and maintain the SLNP structure.

In Figure 7, some lower magnification ADF-STEM images in a series are presented, revealing how the SLNP maintains its size during extensive electron beam induced damage to the surrounding area. Figure 7a shows S vacancies have aggregated into line defects, and by the next frame (Figure 7b), a new nanopore has opened up, red boxed area, and many more line vacancies are formed. Further irradiation leads to more vacancies and nanopores (Figure 7f) plus also the addition of some surface carbon contamination from the STEM imaging. The high defect density and the reduced mobility of S vacancy diffusion from the presence of the surface carbon residue after sequential imaging cause more holes to open up (Figure 7f). During this entire sequence, the size of the SLNP has barely changed, but some restructuring has occurred. Figure 7g–i examines this in more detail and actually shows that the circular SLNP has reverted back to the triangular nanopore form due to interactions with the nearby large hole indicated with the green arrows.

Figure 7 shows that once the density of defects gets sufficiently high, then new holes appear that are larger than the

DOI: 10.1021/acsnano.8b07051
ACS Nano XXXX, XXX, XXX–XXX

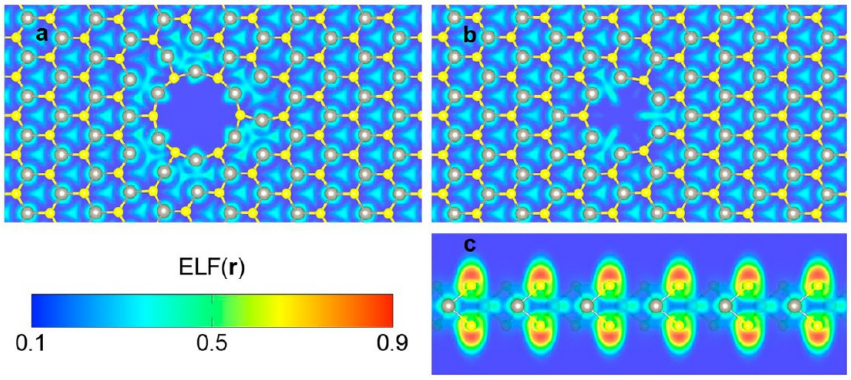

Figure 8. ELF: (a) in the circular SLNP, (b) in the triangular nanopore, and (c) in bulk WS_2, along the (1 1 0) plane. In (a) and (b), the ELF is mapped in a plane containing all W atoms.

SLNP structure. This reveals that during the opening and expansion of other areas during the excessive electron beam irradiation, the SLNP remains relatively consistent. This highlights that it is stable once it forms, to a certain point. However, excessive defect density will always lead to total destruction of a material at some point. At the higher temperatures, the mobility and diffusion of structural defects are bound to get faster, but its speed varies with each temperature (Figure 4). Basically, new S vacancies can be formed at the random positions exposed by electron beam and they can migrate toward line defects and other holes. If there are pre-existing defects such as line defects and some pores, they can affect the formation of nanopores since some defects can be absorbed into relative larger defects. In the Figure 7, there are also pre-existing defects around the circular SLNP. Regardless of that, the circular SLNP is maintained, while other holes indicated by red boxes and some arrows are getting expanded. Therefore, this demonstrates the stability of the circular SLNP compared to new forming nanopores.

Interestingly, when an imperfect circular nanopore is formed as shown in Figure S8, it does not open either for some time, but ends up disappearing. This structure also originates from a triangular nanopore, which indicates a vacancy missing three S pairs and one W atom (Figure S8a), but if the behavior described in Figure 3c,d takes place in only one of the three corners of the triangular nanopore compared to the case of formation of an entire symmetric SLNP (Figure 3), the imperfect circular nanopore is formed as shown in Figure S8b. However, the imperfect circular nanopore is easily absorbed into other structural defects, as shown in Figure S8h, because there are no bond rotations around the pore.

Finally, we have evaluated the electron localization function (ELF),[38,39] for both circular and triangular nanopore structures at the DFT level, in order to rationalize the nature of chemical bonding. The ELF varies from 0 to 1, where 1 corresponds to perfect localization and 0.5 corresponds to the uniform electron gas. Results are presented in Figure 8. For bulk WS_2 (Figure 8c), S sites display large values, while the W sites are characterized by low values, which is a signature of ionic bonding. There is however a certain degree of covalency, as the lobes of the ELF around S sites are oriented toward the neighboring W sites. For both nanopore structures, the degree of bonding between W sites is shown in Figure 8a,b. Some covalency can be observed close to the pore in both cases, as shown by the cyan regions of the ELF connecting two neighboring W sites. These values are however rather low (~0.3−0.4), which shows that the degree of W−W bonding is minimal compared to the W−S bond.

CONCLUSION

By controlling the *in situ* heating temperature from room temperature up to 1000 °C, we show how defect dynamics are influenced by thermal activation of S vacancy diffusion and their relationship to nanopore formation and bond rotations. The midrange temperature of 500 °C was ideal for providing sufficient combination of S vacancy diffusion and defect density build-up to trigger bond rotations and atomic reconstructions due to vacancies, leading to SLNP formation. The SLNPs are formed by reconstruction around a single W vacancy site (triangular nanopore) and remain stable during further irradiation compared to a nonreconstructed sub-nm pore. It is the W−W bonding that helps to achieve stable SLNPs in WS_2. In addition, bond rotations around the SLNP prevent its opening and absorption by other structural defects under electron beam irradiation. This work's comprehensive analysis of the SLNP's detailed atomic bonding arrangement will be of assistance in understanding new structures and local properties of TMDs. The SLNPs are not observed in Mo-based TMDs, such as MoS_2, and suggest that WS_2 might offer advantages in the area of sub-nm pores in 2D materials. The work shows that creating sub-nm pores at different temperatures is important, and future work will explore methods to mass produce SLNPs by combining thermal treatments with scalable production methods such as electrochemical oxidation or ion bombardment.

METHODS

Monolayer WS_2 Chemical Vapor Deposition Synthesis and Transfer. WS_2 monolayers were grown using CVD, based on a previously reported method.[40] A double-walled quartz tube was inserted through two tube furnaces. S precursor powder (300 mg, 99.5%) was placed in the outer tube and aligned with the first furnace. WO_3 (200 mg, 99.9%) precursor was inserted into the inner tube within the second CVD tube furnace, at the center of the hot-zone of the furnace, and the substrate (Si/SiO2 chip) was located in the outer tube with a precalibrated distance further downstream. Ar carrier gas was used to bring reactant vapor to the substrate, permitting WO_3 sulfurization at the substrate. The first, S-containing, furnace was held at 180 °C, and the second furnace at 1170 °C, with the reaction stage taking 3 min. Samples were rapidly cooled by removal from the furnace following the reaction stage.

Transfer was achieved by spin-coating the sample with a supporting poly(methyl acrylate) (PMMA) scaffold (8 wt %, M_w 495k). The PMMA/WS_2 stack was separated from the SiO_2/Si substrate by KOH

DOI: 10.1021/acsnano.8b07051
ACS Nano XXXX, XXX, XXX−XXX

etching (1 M) at 60 °C. The PMMA/WS_2 film was transferred *via* clean glass slides to deionized water to rinse residue from the WS_2 side, which was repeated several times. The film was then transferred to the sample chip, allowed to dry overnight, and then heated on a hot plate at 150 °C to drive off remaining water and promote sample adhesion.

Transmission Electron Microscopy with an *in Situ* Heating Holder. ADF-STEM was conducted using an aberration-corrected JEOL ARM300CF STEM equipped with a JEOL ETA corrector operated at an accelerating voltage of 60 kV located in the electron Physical Sciences Imaging Centre (ePSIC) at Diamond Light Source. Dwell times of 5−20 μs and a pixel size of 0.006 nm px^{-1} were used for imaging with a convergence semiangle of 31.5 mrad, a beam current of 44 pA, and inner-outer acquisition angles of 49.5−198 mrad.

Temperature-dependent ADF-STEM imaging up to 1000 °C was performed using a commercially available *in situ* heating holder from DENS Solutions (SH30-4M-FS). FIB was used to cut open slits in the Si_3N_4 membrane to enable suspended WS_2 samples for imaging. Heating the sample was achieved by passing a current through a platinum resistive coil embedded in the TEM chip (DENS Solutions DENS-C-30). The resistance of the platinum coil was monitored in a four-point configuration, and the temperature was calculated using the Callendar-Van Dusen equation (with calibration constants provided by the manufacturer). Slits were fabricated in the Si_3N_4 membranes using focused ion beam milling before transferring the WS_2.

Image Processing and Simulation. ImageJ was used to process the ADF images. For ADF images, a bandpass filter (between 40 and 3 pixels) was carefully applied to minimize long-range uneven illumination and reduce noise. Multislice image simulations for ADF images were performed using the multislice method implemented in the JEMS software with supercells generated from DFT calculations. Parameters for image simulations were based on the experimental condition of the JEOL ARM300CF. The chromatic aberration at 60 kV is 0.89 mm with an energy spread of 0.42 eV. The probe size is 65 pm, and the convergence semiangle is 31.5 mrad. The angle range for dark-field imaging is from 49.5 to 198 mrad. Spherical aberration is 5 μm.

Density Functional Theory. All *ab initio* calculations were carried out using DFT,[41,42] as implemented in the Vienna *ab Initio* Simulation Package (VASP v5.4)[43,44] and integrated in the MedeA computational environment.[45] Exchange−correlation effects were treated using the generalized gradient approximation (GGA), with the PBE functional developed by Perdew *et al.*[46] The all-electron frozen-core projector augmented wave method (PAW) is employed to solve the Kohn−Sham equations,[47] using plane-wave basis sets with a kinetic energy cutoff of 500 eV.

We have used large 8 × 15 rectangular supercells containing 720 atoms to avoid defect self-interactions. A 20 Å vacuum gap in the direction normal to the monolayer was found enough to avoid artificial interactions between periodic images. The convergence criteria on the energy and atomic forces were, respectively, set to 10^{-5} eV and 10^{-2} eV/Å. Sampling the Γ-point only was found enough to converge the total energy of these large defective systems. In order to minimize compute time, we first relaxed the defective geometries to nonmagnetic ground states. We then performed spin-polarized structure optimizations. While spin-polarization had virtually no effect on the geometries, it non-negligibly affected the total energy of some of the defective structures, giving rise to a nonzero magnetic moment. Finally, we carried out calculations allowing for fully noncollinear magnetism. We obtained identical results as with the spin-polarized model, the relaxed atomic magnetic moments being collinear to the direction normal to the monolayer.

The formation energy of neutral defects E_f can be written as

$$E_f = E_{defect} - E_{pristine} + \sum_i n_i \mu_i$$

where E_{defect} is the energy of the defective structure, $E_{pristine}$ is the energy of the perfect system (here a pristine WS_2 monolayer), and n_i and μ_i are, respectively, the number of atoms and chemical potential of species i removed from the perfect system. W-rich and S-rich environments determine both lower and upper bounds to the μ_W and μ_S chemical potentials.[48] We considered bcc W and α-S as the ground states used to compute μ_W and μ_S at zero temperature.

ASSOCIATED CONTENT

Supporting Information

The Supporting Information is available free of charge on the ACS Publications website at DOI: 10.1021/acsnano.8b07051.

Formation of defects depending on temperatures. Expansion of a triangular nanopore. Trigonal bond rotational defect. Formation energies of nanopores (PDF)

AUTHOR INFORMATION

Corresponding Author

*E-mail: Jamie.warner@materials.ox.ac.uk.

ORCID

Jamie H. Warner: 0000-0002-1271-2019

Notes

The authors declare no competing financial interest.

ACKNOWLEDGMENTS

J.H.W. thanks the support from the Royal Society and the ERC Consolidator grant (725258 CoG 2016 LATO). We thank Diamond Light Source for access and support in use of the electron Physical Science Imaging Centre (EM16854) that contributed to the results presented here. This research used resources of the National Energy Research Scientific Computing Center (NERSC), a U.S. Department of Energy Office of Science User Facility operated under contract no. DE-AC02-05CH11231.

REFERENCES

(1) Jiang, D.; Cooper, V. R.; Dai, S. Porous Graphene as the Ultimate Membrane for Gas Separation. *Nano Lett.* **2009**, *9*, 4019−4024.

(2) Hauser, A. W.; Schwerdtfeger, P. Methane-Selective Nanoporous Graphene Membranes for Gas Purification. *Phys. Chem. Chem. Phys.* **2012**, *14*, 13292−13298.

(3) Schrier, J. Helium Separation Using Porous Graphene Membranes. *J. Phys. Chem. Lett.* **2010**, *1*, 2284−2287.

(4) Nieszporek, K.; Drach, M. Alkane Separation Using Nanoporous Graphene Membranes. *Phys. Chem. Chem. Phys.* **2015**, *17*, 1018−1024.

(5) Drahushuk, L. W.; Strano, M. S. Mechanisms of Gas Permeation through Single Layer Graphene Membranes. *Langmuir* **2012**, *28*, 16671−16678.

(6) Wang, L.; Drahushuk, L. W.; Cantley, L.; Koenig, S. P.; Liu, X.; Pellegrino, J.; Strano, M. S.; Bunch, J. S. Molecular Valves for Controlling Gas Phase Transport Made from Discrete Angström-Sized Pores in Graphene. *Nat. Nanotechnol.* **2015**, *10*, 785.

(7) Surwade, S. P.; Smirnov, S. N.; Vlassiouk, I. V.; Unocic, R. R.; Veith, G. M.; Dai, S.; Mahurin, S. M. Water Desalination Using Nanoporous Single-Layer Graphene. *Nat. Nanotechnol.* **2015**, *10*, 459−464.

(8) Cohen-Tanugi, D.; Grossman, J. C. Water Desalination across Nanoporous Graphene. *Nano Lett.* **2012**, *12*, 3602−3608.

(9) Suk, M. E.; Aluru, N. Water Transport through Ultrathin Graphene. *J. Phys. Chem. Lett.* **2010**, *1*, 1590−1594.

(10) Cohen-Tanugi, D.; Grossman, J. C. Nanoporous Graphene as a Reverse Osmosis Membrane: Recent Insights from Theory and Simulation. *Desalination* **2015**, *366*, 59−70.

(11) Heiranian, M.; Farimani, A. B.; Aluru, N. R. Water Desalination with a Single-Layer MoS_2 Nanopore. *Nat. Commun.* **2015**, *6*, 8616.

DOI: 10.1021/acsnano.8b07051
ACS Nano XXXX, XXX, XXX−XXX

(12) Garaj, S.; Hubbard, W.; Reina, A.; Kong, J.; Branton, D.; Golovchenko, J. Graphene as a Subnanometre Trans-Electrode Membrane. *Nature* **2010**, *467*, 190.
(13) Merchant, C. A.; Healy, K.; Wanunu, M.; Ray, V.; Peterman, N.; Bartel, J.; Fischbein, M. D.; Venta, K.; Luo, Z.; Johnson, A. C.; Drndić, M. DNA Translocation through Graphene Nanopores. *Nano Lett.* **2010**, *10*, 2915−2921.
(14) Garaj, S.; Liu, S.; Golovchenko, J. A.; Branton, D. Molecule-Hugging Graphene Nanopores. *Proc. Natl. Acad. Sci. U. S. A.* **2013**, *110*, 12192−12196.
(15) Venkatesan, B. M.; Bashir, R. Nanopore Sensors for Nucleic Acid Analysis. *Nat. Nanotechnol.* **2011**, *6*, 615.
(16) Wang, Y.; Zheng, D.; Tan, Q.; Wang, M. X.; Gu, L.-Q. Nanopore-Based Detection of Circulating MicroRNAs in Lung Cancer Patients. *Nat. Nanotechnol.* **2011**, *6*, 668.
(17) Feng, J.; Liu, K.; Bulushev, R. D.; Khlybov, S.; Dumcenco, D.; Kis, A.; Radenovic, A. Identification of Single Nucleotides in MoS_2 nanopores. *Nat. Nanotechnol.* **2015**, *10*, 1070.
(18) Farimani, A. B.; Min, K.; Aluru, N. R. DNA Base Detection Using a Single-Layer MoS_2. *ACS Nano* **2014**, *8*, 7914−7922.
(19) Han, Y.; Xu, Z.; Gao, C. Ultrathin Graphene Nanofiltration Membrane for Water Purification. *Adv. Funct. Mater.* **2013**, *23*, 3693−3700.
(20) Du, H.; Li, J.; Zhang, J.; Su, G.; Li, X.; Zhao, Y. Separation of Hydrogen and Nitrogen Gases with Porous Graphene Membrane. *J. Phys. Chem. C* **2011**, *115*, 23261−23266.
(21) Koenig, S. P.; Wang, L.; Pellegrino, J.; Bunch, J. S. Selective Molecular Sieving through Porous Graphene. *Nat. Nanotechnol.* **2012**, *7*, 728.
(22) Lee, Z.; Jeon, K.-J.; Dato, A.; Erni, R.; Richardson, T. J.; Frenklach, M.; Radmilovic, V. Direct Imaging of Soft−Hard Interfaces Enabled by Graphene. *Nano Lett.* **2009**, *9*, 3365−3369.
(23) Sun, L.; Huang, H.; Peng, X. Laminar MoS_2 Membranes for Molecule Separation. *Chem. Commun.* **2013**, *49*, 10718−10720.
(24) Robertson, A. W.; Lee, G.-D.; He, K.; Gong, C.; Chen, Q.; Yoon, E.; Kirkland, A. I.; Warner, J. H. Atomic Structure of Graphene Subnanometer Pores. *ACS Nano* **2015**, *9*, 11599−11607.
(25) Robertson, A. W.; Allen, C. S.; Wu, Y. A.; He, K.; Olivier, J.; Neethling, J.; Kirkland, A. I.; Warner, J. H. Spatial Control of Defect Creation in Graphene at the Nanoscale. *Nat. Commun.* **2012**, *3*, 1144.
(26) He, K.; Robertson, A. W.; Gong, C.; Allen, C. S.; Xu, Q.; Zandbergen, H.; Grossman, J. C.; Kirkland, A. I.; Warner, J. H. Controlled Formation of Closed-Edge Nanopores in Graphene. *Nanoscale* **2015**, *7*, 11602−11610.
(27) Feng, J.; Liu, K.; Graf, M.; Lihter, M.; Bulushev, R. D.; Dumcenco, D.; Alexander, D. T.; Krasnozhon, D.; Vuletic, T.; Kis, A.; Radenovic, A. Electrochemical Reaction in Single Layer MoS_2: Nanopores Opened Atom by Atom. *Nano Lett.* **2015**, *15*, 3431−3438.
(28) O'Hern, S. C.; Boutilier, M. S.; Idrobo, J.-C.; Song, Y.; Kong, J.; Laoui, T.; Atieh, M.; Karnik, R. Selective Ionic Transport through Tunable Subnanometer Pores in Single-Layer Graphene Membranes. *Nano Lett.* **2014**, *14*, 1234−1241.
(29) Lee, J.; Yang, Z.; Zhou, W.; Pennycook, S. J.; Pantelides, S. T.; Chisholm, M. F. Stabilization of Graphene Nanopore. *Microsc. Microanal.* **2014**, *20*, 1732.
(30) Liu, K.; Lihter, M.; Sarathy, A.; Caneva, S.; Qiu, H.; Deiana, D.; Tileli, V.; Alexander, D. T.; Hofmann, S.; Dumcenco, D.; et al. Geometrical Effect in 2D Nanopores. *Nano Lett.* **2017**, *17*, 4223−4230.
(31) Wang, S.; Li, H.; Sawada, H.; Allen, C. S.; Kirkland, A. I.; Grossman, J. C.; Warner, J. H. Atomic Structure and Formation Mechanism of Sub-Nanometer Pores in 2D Monolayer MoS_2. *Nanoscale* **2017**, *9*, 6417−6426.
(32) Yoshimura, A.; Lamparski, M.; Kharche, N.; Meunier, V. First-Principles Simulation of Local Response in Transition Metal Dichalcogenides under Electron Irradiation. *Nanoscale* **2018**, *10*, 2388−2397.
(33) Lin, Y.-C.; Björkman, T.; Komsa, H.-P.; Teng, P.-Y.; Yeh, C.-H.; Huang, F.-S.; Lin, K.-H.; Jadczak, J.; Huang, Y.-S.; Chiu, P.-W.; Suenaga, K. Three-Fold Rotational Defects in Two-Dimensional Transition Metal Dichalcogenides. *Nat. Commun.* **2015**, *6*, 6736.
(34) Komsa, H.-P.; Kurasch, S.; Lehtinen, O.; Kaiser, U.; Krasheninnikov, A. V. From Point to Extended Defects in Two-Dimensional MoS_2: Evolution of Atomic Structure under Electron Irradiation. *Phys. Rev. B: Condens. Matter Mater. Phys.* **2013**, *88*, 035301.
(35) Wang, S.; Lee, G.-D.; Lee, S.; Yoon, E.; Warner, J. H. Detailed Atomic Reconstruction of Extended Line Defects in Monolayer MoS_2. *ACS Nano* **2016**, *10*, 5419−5430.
(36) Ryu, G. H.; Lee, J.; Kim, N. Y.; Lee, Y.; Kim, Y.; Kim, M. J.; Lee, C.; Lee, Z. Line-Defect Mediated Formation of Hole and Mo clusters in Monolayer Molybdenum Disulfide. *2D Mater.* **2016**, *3*, 014002.
(37) Chen, Q.; Li, H.; Zhou, S.; Xu, W.; Chen, J.; Sawada, H.; Allen, C. S.; Kirkland, A. I.; Grossman, J. C.; Warner, J. H. Ultralong 1D Vacancy Channels for Rapid Atomic Migration During 2D Void Formation in Monolayer MoS_2. *ACS Nano*, 2018, Article ASAP, DOI: 10.1021/acsnano.8b01610.
(38) Becke, A. D.; Edgecombe, K. E. A simple measure of electron localization in atomic and molecular systems. *J. Chem. Phys.* **1990**, *92*, 5397−5403.
(39) Savin, A.; Jepsen, O.; Flad, J.; Andersen, O. K.; Preuss, H.; von Schnering, H. G. Electron localization in solid-state structures of the elements: the diamond structure. *Angew. Chem., Int. Ed. Engl.* **1992**, *31*, 187−188.
(40) Rong, Y.; Fan, Y.; Koh, A. L.; Robertson, A. W.; He, K.; Wang, S.; Tan, H.; Sinclair, R.; Warner, J. H. Controlling Sulphur Precursor Addition for Large Single Crystals Domains of WS_2. *Nanoscale* **2014**, *6*, 12096−12103.
(41) Hohenberg, P.; Kohn, W. Inhomogeneous Electron Gas. *Phys. Rev.* **1964**, *136* (3B), B864.
(42) Kohn, W.; Sham, L. J. Self-Consistent Equations Including Exchange and Correlation Effects. *Phys. Rev.* **1965**, *140*, A1133.
(43) Kresse, G.; Hafner, J. Ab Initio Molecular Dynamics for Liquid Metals. *Phys. Rev. B: Condens. Matter Mater. Phys.* **1993**, *47*, 558.
(44) Kresse, G.; Furthmüller, J. Efficiency of Ab-Initio Total Energy Calculations for Metals and Semiconductors Using a Plane-Wave Basis Set. *Comput. Mater. Sci.* **1996**, *6*, 15−50.
(45) *MedeA-2.22*; Materials Design, Inc: San Diego, CA USA, 2018.
(46) Perdew, J. P.; Burke, K.; Ernzerhof, M. Generalized Gradient Approximation Made Simple. *Phys. Rev. Lett.* **1996**, *77*, 3865.
(47) Blöchl, P. E. Projector Augmented-Wave Method. *Phys. Rev. B: Condens. Matter Mater. Phys.* **1994**, *50*, 17953.
(48) Haldar, S.; Vovusha, H.; Yadav, M. K.; Eriksson, O.; Sanyal, B. Systematic Study of Structural, Electronic, and Optical Properties of Atomic-Scale Defects in the Two-Dimensional Transition Metal Dichalcogenides MX_2 (M= Mo, W; X= S, Se, Te). *Phys. Rev. B: Condens. Matter Mater. Phys.* **2015**, *92*, 235408.

DOI: 10.1021/acsnano.8b07051
ACS Nano XXXX, XXX, XXX−XXX